A&A, 708, A225 (2026)
https://doi.org/10.1051/0004-6361/202558208

Astronomy & Astrophysics

Sub-second cadence structure of optical flares on AD Leo

B. Schmercz[1,2,3,⋆], B. Seli[1,2,3], K. Vida[1,2], L. Kriskovics[1,2], A. Görgei[1,2,3], K. Oláh[1,2], and Zs. Regály[1,2]

[1] Konkoly Observatory, HUN-REN Research Centre for Astronomy and Earth Sciences, Konkoly Thege út 15-17, H-1121 Budapest, Hungary
[2] HUN-REN RCAES, MTA Centre of Excellence, Budapest, Konkoly Thege út 15-17, H-1121 Budapest, Hungary
[3] Eötvös University, Department of Astronomy, Pf. 32, 1518 Budapest, Hungary

Received 21 November 2025 / Accepted 22 February 2026

ABSTRACT

Context. Stellar flares are sudden brightenings caused by magnetic reconnection and are frequently observed on late-type stars. High-cadence photometry of flares provides valuable insights into the mechanisms of these events, yet such observations remain scarce.
Aims. We seek to explore the sub-second fine structure of stellar flares and assess the information content in high-speed photometry.
Methods. New 0.3 s-cadence photometry from a six-year-long observing campaign of the active M-dwarf AD Leo is presented. We use time–frequency analysis to detect quasi-periodic pulsations in the decay phase of flares. We explore statistical measures of time-series complexity of the detected flares to quantify the information gain achievable with high-cadence photometry.
Results. We detect 42 flares in 211 hours of observations. The flare frequency distribution is consistent with the previous literature. We find no quasi-periodic pulsations with periods below a few seconds, and identify two candidate signals with periods around 1 and 3 min. Using different measures of complexity on the binned flare light curves, we confirm the advantages of high observing cadence. However, we also find a plateau up to a binning of ≈4−5 s for a few complex flares, suggesting that an exposure time of a few seconds is usually enough to retain most of the information carried by a single-filter observation.
Conclusions. New photometric observations of AD Leo revealed sub-structures of flare light curves on a timescale of a few seconds, but we found no features on timescales below that.

Key words. stars: activity – stars: flare – stars: late-type – stars: individual: AD Leo

1. Introduction

Stellar flares are caused by the sudden release of magnetic energy in stellar atmospheres, which is observable as an increase in stellar luminosity for minutes to hours (Kowalski 2024). With the advent of space-borne photometry, hundreds of thousands of flares have been observed with a few minutes' cadence (e.g., Yang & Liu 2019; Feinstein et al. 2022; Lin et al. 2024; Seli et al. 2025). However, flare observations with sub-second time resolution are relatively rare. One of the early experiments was the work of Beskin et al. (1988a), who used a 6-m telescope equipped with the Multichannel Analysis of Nanosecond Intensity Alterations (MANIA) instrument, capable of detecting individual photon arrival times with an accuracy of 0.3 µs. They detected 118 flares on eight stars in 35 hours of observations. They found no fine structure on timescales shorter than 0.1 s, and only detected statistically significant variations on timescales longer than 0.5 s. More details of these observations were published by Beskin et al. (1988b), including light curves showing flares with different morphologies, such as double peaks and possible oscillations. Most of these events are shorter than 1 min. High-cadence observations also enable the detection of quasi-periodic pulsations (QPPs; Zimovets et al. 2021). Panferov et al. (2024) used the MANIA instrument to detect 157 flares on M dwarfs in 70 hours of observations. The 1 s time resolution allowed them to find 13 QPPs, with periods ranging from 6 to 107 s. High-cadence observations were also carried out by Aizawa et al. (2022), who observed 22 flares on M dwarfs with 1 s cadence. They note the presence of flat peaks, which are rarely resolved with longer cadence, and provide a new analytical flare template.

A few studies focused on detecting flares with the shortest possible duration, analogous to solar micro- and nanoflares. Robinson et al. (1995) used the *Hubble* Space Telescope to observe CN Leo in the ultraviolet, finding 32 flare-like events, most of which lasted for less than 10 s. Tovmassian et al. (1997) reported impulsive events with a duration of less than 1 s, mostly following longer flares. Schmitt et al. (2016) observed UV Cet with 4 µs time resolution and found two flares with rise and decay times of 2 s.

AD Leo (GJ 388) is one of the brightest and most active flare stars, making it an ideal target in the hunt for stellar flares. It has a spectral type of M3V, a rotational period of 2.227 days, and it is probably viewed pole-on (Kossakowski et al. 2022). AD Leo is a prime target for searching for spectral signatures of flares (Hawley & Pettersen 1991; Namekata et al. 2020; Muheki et al. 2020) and radio bursts (Osten & Bastian 2006; Zhang et al. 2023; Mohan et al. 2024). The evolution of its magnetic field has been followed with spectropolarimetric observations (Morin et al. 2008; Lavail et al. 2018; Bellotti et al. 2023). AD Leo has a long history of photometric observations of its flare activity (e.g., Abell 1959; Szeidl 1969; Pettersen et al. 1984; Hawley et al. 2003; Dal & Evren 2010, among many others), including multicolor fast photometric observations (Lovkaya 2013) and more recent space photometric studies with MOST (Hunt-Walker et al. 2012), TESS (Bai et al. 2023; Ram et al. 2025), and CHEOPS (Bruno et al. 2024).

In this paper we present new fast photometric observations of AD Leo and aim to identify fine structure in stellar flare light

⋆ Corresponding author: schmercz.blanka@csfk.org

curves, in order to find the shortest timescale where any kind of variation can be expected.

2. Data

Observations were carried out at Piszkéstető Mountain Station, Konkoly Observatory, using the 1-meter Ritchey–Chrétien–Coudé telescope ($D = 1.02$ m, $f = 13.8$ m), which provides a field of view of approximately 3.5 arcmin.

Observations were performed with OCELOT (Optical Camera with ELectronmultiplying OutpuT), an Andor iXon+888 back-illuminated electron multiplying charge-coupled device (EMCCD) camera in a custom casing for temperature control, using a Johnson B filter, with a cadence of 0.286 s, operating at −80°C. An EMCCD camera is capable of achieving fast sampling with negligible readout time in frame transfer mode, and it can reliably detect photons even under low light conditions (Smith et al. 2004). We selected the shortest available exposure time for the 16-bit mode with 4×4 binning that still allowed the field of view needed to include a comparison star. Measurements were carried out on 49 nights between February 23, 2019, and April 4, 2025 (see the full observing log in Table C.1). In total, approximately 211 hours of observational data were collected.

Data reduction was performed using differential aperture photometry routines implemented with `photutils` (Bradley et al. 2025) and `astropy` (Astropy Collaboration 2022), following dark subtraction and flat-field correction. BD+20 2464 was used as the comparison star, which has a magnitude of 11.67 in the B filter (Høg et al. 2000).

The noise level of the light curve is generally high (0.05 mag on average; see Table C.1), and it also depends on sky conditions. This is partly a consequence of the limited signal transmitted through the Johnson B filter, which we used to maximize the flare signal (see, e.g., Bicz et al. 2025). For visual aid in the figures, we enhance the details with smoothing.

3. Methods

3.1. Flare energies

Flare energies were estimated using the method described in Oláh et al. (2022). This approach is based on the concept of equivalent duration (ED; Gershberg 1972), which represents the time that a star in its quiescent state requires to emit the same amount of energy that is released during a flare. The ED is calculated as the integral of the relative flare intensity over its duration:

$$\mathrm{ED} = \int_{t_1}^{t_2} \left(\frac{I(t)}{I_0} - 1 \right) \mathrm{d}t, \tag{1}$$

where $I(t)$ is the observed stellar intensity as a function of time, and I_0 denotes the quiescent (non-flaring) intensity level. To estimate the uncertainties of the EDs, we slightly varied the integration limits and examined the resulting changes.

The flare energies were then calculated by multiplying the EDs by the quiescent B-band luminosity (L_B). To estimate L_B we used a BT-NextGen model spectrum (Hauschildt et al. 1999) for AD Leo with $T_{\mathrm{eff}} = 3400$ K, $\log g = 4.5$ and $[\mathrm{Fe/H}] = 0$, and the B filter transmission curve. We determined the fraction of the model spectrum transmitted through the filter and multiplied it by the bolometric luminosity of the star from Favata et al. (2000) to derive the quiescent B-band luminosity of $L_B = 1.23 \times 10^{30}$ erg s^{-1}.

To make the flare energies easier to compare with previous studies, the B-band energies were converted to bolometric values by assuming a blackbody flare temperature of 12 000 K (Bai et al. 2023). As there is a large scatter in measured flare temperatures (see, e.g., Rabello Soares et al. 2022), we estimate the uncertainty of the conversion by assuming a standard deviation of 3000 K. Integrating a black body flare spectrum with the B filter transmission curve results in a ratio of the bolometric to B-band energies of 7.69 ± 1.78, thus giving

$$E_{\mathrm{bol}} = (7.69 \pm 1.78) \times L_B \times \mathrm{ED}. \tag{2}$$

If $\mathrm{d}N$ represents the number of flares that occur within the energy interval $E + \mathrm{d}E$, the flare energy distribution follows a power-law relation (see, e.g., Kowalski 2024):

$$\frac{\mathrm{d}N}{\mathrm{d}E} \propto E^{-\alpha}. \tag{3}$$

Integrating the relation gives the cumulative flare frequency distribution in logarithmic form:

$$\log \nu = \beta \log E + a, \tag{4}$$

where ν is the cumulative frequency of flares with energy greater than E, and $\beta = 1 - \alpha$. The index α characterizes the energy distribution: for $\alpha > 2$, low-energy flares dominate the total output; for $\alpha < 2$, high-energy flares contribute more (Hudson 1991).

3.2. Identifying quasi-periodic pulsations

To search for QPPs in complex flare light curves, different methods can be used in both the time and frequency domains (Broomhall et al. 2019). Here, we use a modified version of the short-term Fourier transform (STFT).

In the STFT approach, the signal is multiplied by a Gaussian window centered at a given time, and the resulting segment is Fourier-transformed to extract the local frequency content. By sliding the window along the time axis, a time–frequency representation is produced, which can be visualized as a two-dimensional map when the window positions are sampled densely (Kolláth & Oláh 2009).

In the modified version used here from the `seismolab` package (Bódi 2024), local frequency analysis is performed using the Lomb–Scargle periodogram instead of the standard Fourier transform. This approach is known as the windowed Lomb–Scargle transform. As these methods work best with stationary baselines, we first subtract the flare profile using a Savitzky–Golay filter (Savitzky & Golay 1964). This smoothing algorithm fits low-order polynomials to successive local data segments, effectively reducing noise while preserving sharp features and peak structures. For smoothing, we adopted a kernel size of 3 min. Subsequently, for the windowed Lomb–Scargle transform of each flare, we applied a Gaussian window with a width of 1.2 min.

The significance of potential signals was evaluated using a bootstrap procedure, similar to López-Santiago et al. (2026). We generated 10 000 surrogate light curves by randomly permuting the normalized residuals obtained after subtracting a smoothed version of the original light curve. The signal significance was then estimated from the distribution of the resulting maximum peak amplitudes. This method assumes white noise as the null hypothesis, so the significance we get can be overly optimistic if correlated noise is present.

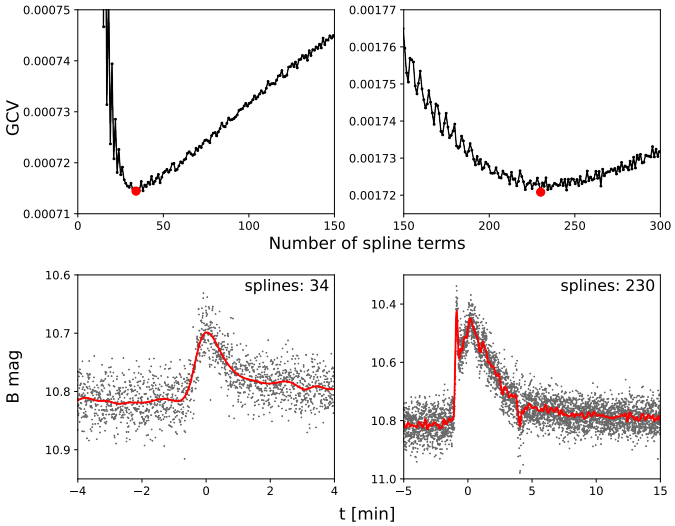

Fig. 1. Complexity assessment with GAMs for two flares. Top: GCV score as a function of the number of spline terms, with the red point marking the minimum. Bottom: Flares with the best-fitting curve corresponding to this minimum; associated spline values are indicated in the panels.

3.3. Measure of complexity

High-cadence photometry can reveal details of flares that cannot be seen with longer integration times (see, e.g., Yang et al. 2018; Howard & MacGregor 2022). In this section, we try to quantify this information gain by using different methods to measure the "complexity" of light curve segments containing flares. We aim to find a metric that is non-parametric (i.e., it does not assume a functional form for components), robust to random noise, and does not depend only on the number of points in the light curve segment, making the metric comparable across different flares. For example, we expect a single-peaked flare to have a low complexity score, while a flare with multiple peaks or QPPs should have a higher score, regardless of its amplitude and duration. We will use these techniques to rank the flares in the sample from least to most complex and to see how the complexity of the flares changes with binning, simulating different integration times. In this way, we can find an optimal integration time that maximizes the signal-to-noise ratio while still preserving the information content of the stellar flare light curve – for the first time with real data.

We first assessed flare complexity using generalized additive models (GAMs; Hastie & Tibshirani 1986) via `pyGAM` (Servén & Brummitt 2018), which extend linear models with smooth functions using penalized B-splines. The flexibility of these functions is controlled by the number of spline terms through the number and placement of knots, determining how finely non-linear patterns are captured. For each flare, the segment of the time series to be fitted was predefined, spanning from a few minutes before the flare onset to a few minutes after its end. Each flare was then fitted using a number of spline terms ranging from 4 to 400, while all other model parameters were kept at their default values. The resulting fits were evaluated using the generalized cross-validation (GCV) score, which estimates the model's prediction error while balancing fit quality and model complexity. This helps to avoid overfitting by penalizing overly complex models. Since lower GCV values indicate better fits, the value corresponding to the minimum GCV was adopted as the measure of model complexity, as illustrated in Fig. 1. This method is easy to interpret and works well with noisy data, as GAMs are often applied to smooth and interpolate noisy datasets (see, e.g., Csörnyei et al. 2023; Brandt et al. 2024).

The second method involves the effective degrees of freedom (EDFs) from a GAM fit, computed with a fixed number of spline terms. The EDF depends on the number of GAM parameters and also on the smoothing penalty, so its value is generally not an integer. Using a fixed number of spline terms is necessary to compare the EDF across different events, but it risks underfitting for larger flares or overfitting for smaller ones. We used 100 spline terms, which gives a reasonable fit for all flares.

Increment entropy provides an alternative way to quantify dataset complexity (Liu et al. 2016). It measures the complexity of time series data by calculating the Shannon entropy of patterns derived from the increments (differences) between consecutive data points. The metric was computed using the `EntropyHub` toolkit (Flood & Grimm 2021), which analyzes the distribution of increments between consecutive data points encoded as symbolic patterns. Higher values reflect greater variability and less predictable changes.

4. Results and discussion

4.1. Flare detection

A total of 42 flare events were identified through visual inspection of the light curve, as shown in Fig. A.1. For each flare, the light curve was fitted with the flare profile described in Davenport et al. (2014). The resulting parameters (peak time, amplitude, and $t_{1/2}$ full width at half maximum) are listed in Table D.1, along with the three complexity metrics. The table also gives the corresponding B-band and bolometric flare energies, along with their uncertainties obtained by propagating the errors in the flare temperature and the EDs.

4.2. Flare frequency distribution

The flare frequency distribution (FFD) of AD Leo was determined and the following power law was fitted for energies greater than $E_{\rm bol} = 6.8 \times 10^{31}$ erg (corresponding to the minimum energy at which the $E_{\rm min}$–slope function flattens, similar to the method of Petrucci et al. 2024):

$$\log \nu = (-0.70 \pm 0.02) \log E_{\rm bol} + (22.5 \pm 0.5), \quad (5)$$

resulting in $\alpha = 1.70 \pm 0.02$. This FFD, together with the fitted line, is shown in Fig. 2. For context, the figure also includes previously published FFDs from the literature, with all energies converted to bolometric values for direct comparison. Potential temporal variations in the FFD are not addressed in this study due to the lack of sufficiently-extensive data.

Earlier FFDs of AD Leo show a range of slopes, generally consistent with our result. Lacy et al. (1976) reported $\alpha = 1.82 \pm 0.27$, although it was based on just nine flares observed over 21.5 hours. Gershberg & Shakhovskaia (1983), with over 1000 hours of monitoring and 54 flares, found a flatter slope of $\alpha = 1.48 \pm 0.06$. Pettersen et al. (1984) observed the star over several years and reported $\alpha = 1.62 \pm 0.09$, finding no significant year-to-year variations. Hunt-Walker et al. (2012) identified 19 flares in about 140 hours of continuous photometry, yielding $\alpha = 1.68 \pm 0.16$. More recently, Bai et al. (2023) found $\alpha = 1.78 \pm 0.09$ from TESS and $\alpha = 1.44 \pm 0.15$ from GWAC-F30, although the latter was based on only nine events. In addition, Ram et al. (2025) compared nine different α values obtained from both

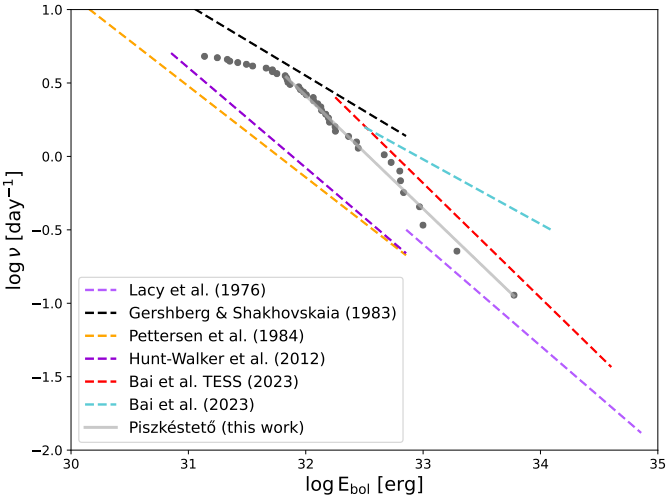

Fig. 2. FFD derived in this work (gray data points and corresponding best-fit line), compared to fitted trends reported in the literature.

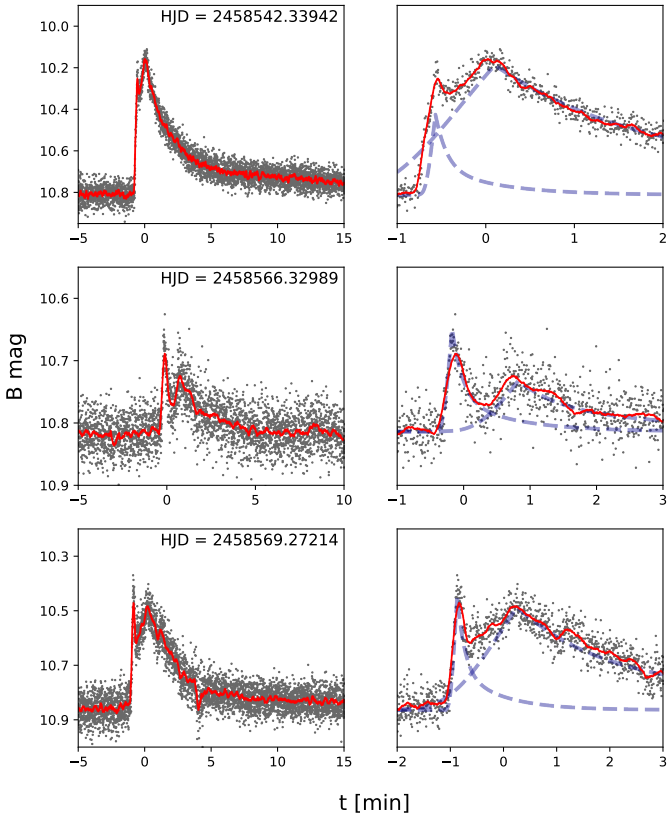

Fig. 3. Light curves of flares exhibiting complex temporal structures are shown as gray points, with the corresponding smoothed curves indicated by red lines. The first column shows the full flare profiles, while the second column provides magnified views of the peaks, illustrating the two fitted flare components with dashed lines. The HJD indicated in each panel of the first column corresponds to $t = 0$ on the time axis.

photometric and spectroscopic observations. Here we limit our comparison to photometric results.

The efficiency of flare detection and the accuracy of flare energy estimation are both affected by the exposure time (Yang et al. 2018). To investigate how information derived from flare observations, for example, FFD, depends on exposure time, the dataset was re-binned using bin sizes ranging from 1.2 s to 5 min. A flare was considered detected if it contained at least five data points and its peak exceeded the quiescent level by more than three standard deviations. The quiescent level and its standard deviation for each bin size were estimated by repeatedly re-binning the data with shifted bin starting points. The EDs and the FFD were then computed for each bin size. The ED of individual flares, as well as the location of the break point due to the low completeness and the overall shape of the FFD, remained nearly constant across all bin sizes. However, with larger bins, fewer flares were detected, and around 2.5 min the break point itself disappeared, leaving only the high-energy region. We note that this analysis assumed zero readout time. A non-negligible readout time could bias the ED of complex flares.

4.3. Multi-peak flares

Complex flares exhibiting multiple peaks are often interpreted as sequences of rapidly successive simple flare events (e.g., Davenport et al. 2014; Vida et al. 2016), a phenomenon that is also well documented on the Sun. Possible explanations include homologous flares, in which successive eruptions originate within the same active region and involve similar magnetic structures (Ellison 1963), and sympathetic flares, in which activity in one region can trigger flares in another through large-scale magnetic connections (Török et al. 2011). Both processes have been observed on the Sun (e.g., Polito et al. 2017; Yang et al. 2025; Guité et al. 2025), but the limited spatial resolution of stellar observations prevents us from distinguishing between them. Several mechanisms have been proposed to explain this behavior (e.g., Mullan 1976; Wang et al. 2001), although the precise cause remains a subject of ongoing investigation.

In our sample, three flares displayed this complex behavior. The light curves of these complex flares are presented in Fig. 3, with the time difference between successive peaks being less than two minutes in each case. Considering that 42 flares were detected during 211 hours of observation, the probability that, in these three cases, the two peaks that represent separate flares occurred independently despite being so close together is very low. When each complex flare was decomposed into two events using the flare template of Davenport et al. (2014), the first event was generally shorter than the second, as reflected in its lower $t_{1/2}$ value, and for the flares at HJD = 2458566.32989 and HJD = 2458569.27214, the first event also reached a higher amplitude than the second. We also note that in these cases, the peak of the first component lies close to where the rise phase of the second component begins (see the right-hand panels of Fig. 3). Flares with similar morphologies often appear among complex flares (see, e.g., Fig. 8 in Aizawa et al. 2022, Fig. 10 in Howard & MacGregor 2022, Fig. 5 in Valluvan et al. 2024, or Fig. 1 in Yudovich et al. 2025).

4.4. Quasi-periodic pulsations

To look for QPPs with periods between 0.6 s and 10 min, we checked the windowed Lomb–Scargle transform for the decay phase of each flare. Based on tests with artificial signals injected into real flares, periods within this range can be reliably identified, provided that the signal is sufficiently long (i.e., it lasts for at least a few cycles). We identified two strong signals: one with a period of approximately 1 min and a significance of 6.1σ, and another with a period of about 3 min and a significance of 6.8σ.

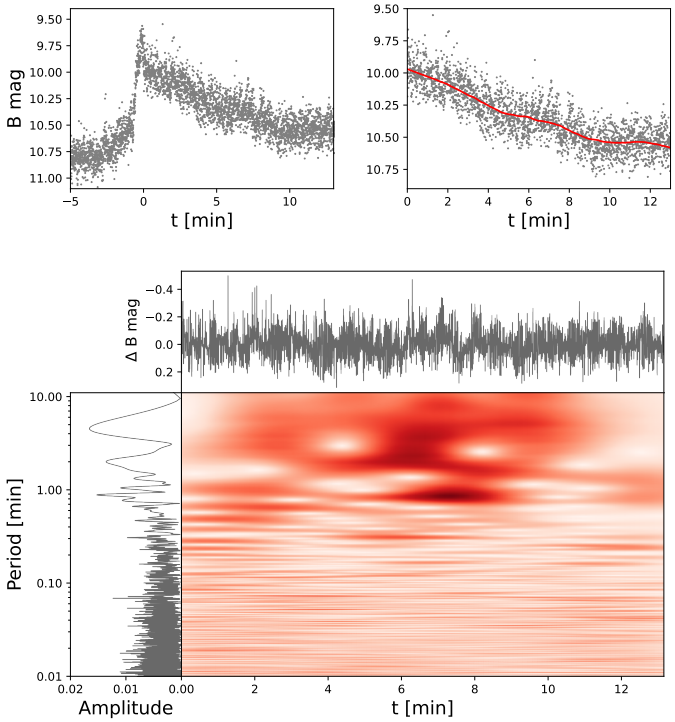

Fig. 4. Time–frequency analysis of the flare at HJD = 2458564.51777. Red line in the upper right panel shows the smoothed light curve that was subtracted before the application of the windowed Lomb–Scargle periodogram. A possible QPP is present with a period around 1 min (around $t = 6-8$ min).

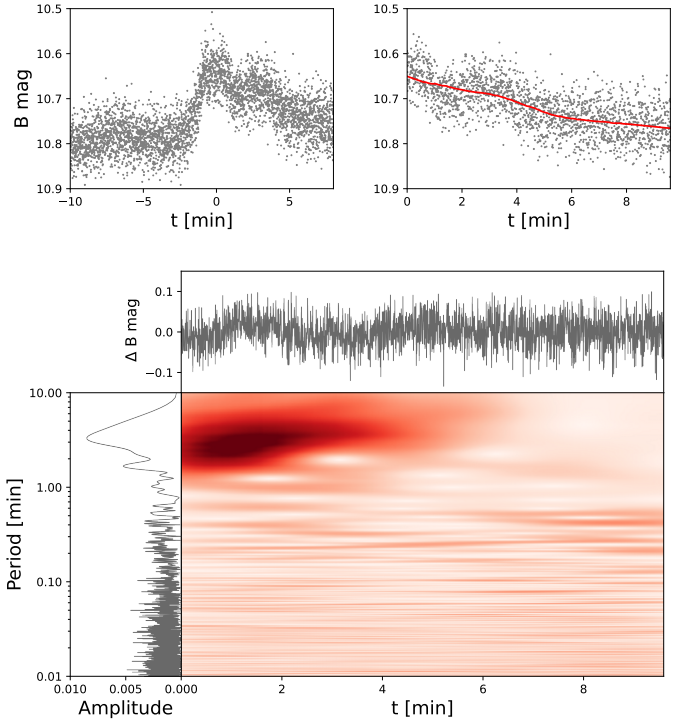

Fig. 5. Same as Fig. 4 for the flare at HJD = 2458567.44626. Possible QPP is present with a period around 3 min.

These cases are shown in Figs. 4 and 5. No QPP with periods on the order of a few seconds was found.

Most QPP detections reported in the literature have periods similar to those of the candidates identified here. Panferov et al. (2024) detected 13 QPPs with 1 s temporal resolution, with periods between 6 and 107 s. Howard & MacGregor (2022) found 49 QPP candidates with periods ranging from 2 to 36 min, using 20 s cadence TESS data. Using more sectors of TESS 20 s observations, Joshi et al. (2025) extended the list with 61 QPPs, with periods between 42 and 193 s. QPPs on the Sun are observed down to periods of a few seconds (Zimovets et al. 2021). Zaitsev et al. (2004) studied a radio flare on AD Leo, and found a QPP-like signal with a period smoothly changing from 0.5 to 5 s, and interpreted it in the context of magnetohydrodynamic oscillations.

4.5. Quantifying flare complexity

Flare complexity was quantified using the methods outlined in Sect. 3.3. To estimate the errors, for each flare we took data segments of the same length as the original, shifted their starting points by a few seconds (±1 s, ±3 s, ±5 s, ±10 s, ±30 s), recalculated the given quantity for each, and finally took the standard deviation of all these values. For the method based on the number of spline terms required for the best GAM fit, the errors were rounded up to the nearest higher integer (since the GAM-based approach can only yield integer values). The complexity values derived from the original unbinned dataset, together with their estimated errors, are listed in Table D.1.

We first used these methods to compare different flares in the sample, and then to examine how temporal binning affects the values for individual flares. All 42 flares were treated as detected at all bin sizes, although in reality smaller flares might not be identifiable at lower temporal resolution.

As expected, short, low-amplitude flares ranked lowest in complexity, whereas long, high-amplitude flares exhibiting multiple peaks (e.g., the red and orange curves in Fig. 6, top and bottom panels in Fig. 3, respectively) or QPPs (e.g., the blue curve in Fig. 6, top panels in Fig. 4) ranked highest. The spline-count method from the GAM fit was particularly effective: unlike the other methods, which were strongly amplitude-dependent and placed the flare at the HJD = 2458566.32989 mid-range (see the middle panel of Fig. 3), it correctly identified it as one of the most complex due to its multiple peaks.

Flare complexity was analyzed as a function of exposure time by assessing the performance of the ranking and the changes in complexity values in the bin sizes from 1.2 s to 3 min. The EDF-based GAM method provided the most consistent flare ranking, maintaining reliable sorting up to 3 min bins. Increment entropy remained effective up to about 2.5 min, whereas the spline-count GAM method performed well only at small bin sizes (around 0.5 min). As expected, the complexity values of individual flares decreased rapidly with binning across all methods (see Fig. 6). However, the spline-count GAM method revealed an interesting behavior for double-peaked flares: for the two larger cases (top and bottom panels in Fig. 3, red and orange curves in Fig. 6, respectively), the complexity remained nearly constant up to a bin size of approximately 4–5 s, after which it dropped sharply. Such a plateau is visible for some of the less complex flares as well, suggesting that an integration time of a few seconds does not result in a significant loss of information and indicating that there is likely no fine structure on shorter timescales in this dataset. However, the high noise level of the light curve also hinders the detection of short-lived and low-amplitude signals.

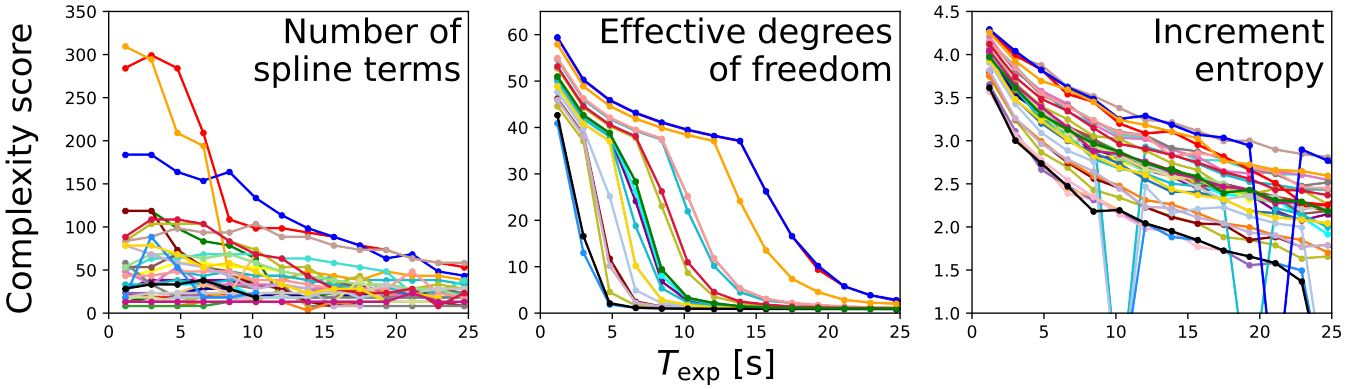

Fig. 6. Variation in complexity scores with different bin sizes for the three complexity analysis methods. Each colored line corresponds to a different flare. See the text for details.

We can also explore the relationships between the six available parameters for the 42 flares in the sample: amplitude, $t_{1/2}$, bolometric energy, and the three measures of complexity. Based on the Spearman rank correlation coefficient, which measures the strength of general monotonic relationships, there is a strong correlation between the EDF and increment entropy, but the relationship between these parameters and the number of spline terms in the GAM fit is weak. The complexity metrics show only moderate correlations with the amplitude and $t_{1/2}$, indicating that they are indeed independent parameters. The pairwise correlations can be seen in Fig. B.1.

5. Conclusions

Using high-cadence photometry, we studied the M dwarf AD Leo. From our analysis, the following conclusions can be drawn:

- Using 0.3 s-cadence *B*-band photometry, in 211 hours of observations over 49 nights between 2019 and 2025, we identified 42 flare events.
- The flare energy distribution follows a power law with a slope of $\alpha = 1.70 \pm 0.02$, consistent with earlier results.
- Three flares showed multi-peak structures suggesting a complex magnetic energy release.
- In the case of two events, we found indications of quasi-periodic pulsations in the decay phase of the flares with periods around 1 and 3 min. No QPP signal was found on the timescale of a few seconds.
- Based on different complexity measures, we found that the information content of complex flares remains largely preserved up to a binning size of ≈4–5 s.

These results can provide practical guidance for planning future observations and space missions capable of fast sampling, for example, the VISPhot instrument of Ariel (Tinetti et al. 2018). Also, the flare complexity metrics presented here can be used in future studies to describe the temporal morphology of flares in large photometric catalogs and to rank events based on their complexity.

Data availability

The full observed light curve of AD Leo is available at the CDS via https://cdsarc.cds.unistra.fr/viz-bin/cat/J/A+A/708/A225

Acknowledgements. We thank the anonymous reviewer for improving the manuscript with helpful suggestions. This work was supported by the Hungarian National Research, Development and Innovation Office Élvonal grant KKP-143986. SB thanks the financial support provided by the undergraduate research assistant program of Konkoly Observatory. This research was also supported by the EKÖP-24 University Excellence Scholarship Program of the Ministry for Culture and Innovation, from the source of the National Research, Development and Innovation Fund. On behalf of the "*Looking for stellar CMEs on different wavelengths*" project we are grateful for the possibility of using HUN-REN Cloud (Héder et al. 2022) which helped us achieve the results published in this paper.

References

Abell, G. O. 1959, PASP, 71, 517
Aizawa, M., Kawana, K., Kashiyama, K., et al. 2022, PASJ, 74, 1069
Astropy Collaboration (Price-Whelan, A. M., et al.) 2022, ApJ, 935, 167
Bai, J.-Y., Wang, J., Li, H. L., et al. 2023, PASP, 135, 064201
Bellotti, S., Morin, J., Lehmann, L. T., et al. 2023, A&A, 676, A56
Beskin, G. M., Chekh, S. A., Gershberg, R. E., et al. 1988a, Sov. Astron. Lett., 14, 65
Beskin, G. M., Gershberg, R. E., Neizvestnyi, S. I., et al. 1988b, Bull. Crimean Astrophys. Obs., 79, 67
Bicz, K., Falewicz, R., Heinzel, P., et al. 2025, A&A, 699, A90
Bódi, A. 2024, J. Open Source Softw., 9, 7118
Bradley, L., Sipőcz, B., Robitaille, T., et al. 2025, https://doi.org/10.5281/zenodo.14889440
Brandt, D. A., Vega, E. F., & Ridley, A. J. 2024, Space Weather, 22, e2023SW003680
Broomhall, A.-M., Davenport, J. R. A., Hayes, L. A., et al. 2019, ApJS, 244, 44
Bruno, G., Pagano, I., Scandariato, G., et al. 2024, A&A, 686, A239
Csörnyei, G., Anderson, R. I., Vogl, C., et al. 2023, A&A, 678, A44
Dal, H. A., & Evren, S. 2010, AJ, 140, 483
Davenport, J. R. A., Hawley, S. L., Hebb, L., et al. 2014, ApJ, 797, 122
Ellison, M. A. 1963, QJRAS, 4, 62
Favata, F., Micela, G., & Reale, F. 2000, A&A, 354, 1021
Feinstein, A. D., Seligman, D. Z., Günther, M. N., & Adams, F. C. 2022, ApJ, 925, L9
Flood, M. W., & Grimm, B. 2021, PLoS ONE, 16, e0259448
Gershberg, R. E. 1972, Ap&SS, 19, 75
Gershberg, R. E., & Shakhovskaia, N. I. 1983, Ap&SS, 95, 235
Guité, L. S., Strugarek, A., & Charbonneau, P. 2025, A&A, 694, A74
Hastie, T., & Tibshirani, R. 1986, Stat. Sci., 1, 297
Hauschildt, P. H., Allard, F., & Baron, E. 1999, ApJ, 512, 377
Hawley, S. L., & Pettersen, B. R. 1991, ApJ, 378, 725
Hawley, S. L., Allred, J. C., Johns-Krull, C. M., et al. 2003, ApJ, 597, 535
Héder, M., Rigó, E., Medgyesi, D., et al. 2022, Információs Társadalom, 22, 128
Høg, E., Fabricius, C., Makarov, V. V., et al. 2000, A&A, 355, L27
Howard, W. S., & MacGregor, M. A. 2022, ApJ, 926, 204
Hudson, H. S. 1991, Sol. Phys., 133, 357
Hunt-Walker, N. M., Hilton, E. J., Kowalski, A. F., Hawley, S. L., & Matthews, J. M. 2012, PASP, 124, 545
Joshi, A., Van Doorsselaere, T., Lim, D., & Fritzewski, D. J. 2025, A&A, 700, A178
Kolláth, Z., & Oláh, K. 2009, A&A, 501, 695

Kossakowski, D., Kürster, M., Henning, T., et al. 2022, A&A, 666, A143
Kowalski, A. F. 2024, Liv. Rev. Sol. Phys., 21, 1
Lacy, C. H., Moffett, T. J., & Evans, D. S. 1976, ApJS, 30, 85
Lavail, A., Kochukhov, O., & Wade, G. A. 2018, MNRAS, 479, 4836
Lin, C.-L., Apai, D., Giampapa, M. S., & Ip, W.-H. 2024, AJ, 168, 234
Liu, X., Jiang, A., Xu, N., & Xue, J. 2016, Entropy, 18, 22
López-Santiago, J., Reale, F., Micela, G., et al. 2026, MNRAS, 546, staf2256
Lovkaya, M. N. 2013, Astron. Rep., 57, 603
Mohan, A., Mondal, S., Wedemeyer, S., & Gopalswamy, N. 2024, A&A, 686, A51
Morin, J., Donati, J. F., Petit, P., et al. 2008, MNRAS, 390, 567
Muheki, P., Guenther, E. W., Mutabazi, T., & Jurua, E. 2020, A&A, 637, A13
Mullan, D. J. 1976, ApJ, 204, 530
Namekata, K., Maehara, H., Sasaki, R., et al. 2020, PASJ, 72, 68
Oláh, K., Seli, B., Kővári, Z., Kriskovics, L., & Vida, K. 2022, A&A, 668, A101
Osten, R. A., & Bastian, T. S. 2006, ApJ, 637, 1016
Panferov, A., Beskin, G., Karpov, S., & Maryeva, O. 2024, ArXiv e-prints [arXiv:2412.07580]
Petrucci, R. P., Gómez Maqueo Chew, Y., Jofré, E., Segura, A., & Ferrero, L. V. 2024, MNRAS, 527, 8290
Pettersen, B. R., Coleman, L. A., & Evans, D. S. 1984, ApJS, 54, 375
Polito, V., Del Zanna, G., Valori, G., et al. 2017, A&A, 601, A39
Rabello Soares, M. C., de Freitas, M. C., & Ferreira, B. P. L. 2022, AJ, 164, 223
Ram, D., Mondal, S., Patra, D., Ghosh, S., & Khumbhakar, R. 2025, ApJ, 980, 196
Robinson, R. D., Carpenter, K. G., Percival, J. W., & Bookbinder, J. A. 1995, ApJ, 451, 795
Savitzky, A., & Golay, M. J. E. 1964, Anal. Chem., 36, 1627
Schmitt, J. H. M. M., Kanbach, G., Rau, A., & Steinle, H. 2016, A&A, 589, A48
Seli, B., Vida, K., Oláh, K., et al. 2025, A&A, 694, A161
Servén, D., & Brummitt, C. 2018, https://doi.org/10.5281/zenodo.1208724
Smith, N., Coates, C., Giltinan, A., et al. 2004, SPIE Conf. Ser., 5499, 162
Szeidl, B. 1969, Inf. Bull. Var. Stars, 345, 2
Tinetti, G., Drossart, P., Eccleston, P., et al. 2018, Exp. Astron., 46, 135
Török, T., Panasenco, O., Titov, V. S., et al. 2011, ApJ, 739, L63
Tovmassian, H. M., Recillas, E., Cardona, O., & Zalinian, V. P. 1997, Rev. Mex. Astron. Astrofis., 33, 107
Valluvan, A. B., Goyal, A., Jain, D., et al. 2024, Sol. Phys., 299, 8
Vida, K., Kriskovics, L., Oláh, K., et al. 2016, A&A, 590, A11
Wang, H., Chae, J., Yurchyshyn, V., et al. 2001, ApJ, 559, 1171
Yang, H., & Liu, J. 2019, ApJS, 241, 29
Yang, H., Liu, J., Qiao, E., et al. 2018, ApJ, 859, 87
Yang, S., Zheng, R., Hou, Y., et al. 2025, A&A, 698, A185
Yudovich, D. G., Yang, K. E., & Sun, X. 2025, ApJ, 984, 186
Zaitsev, V. V., Kislyakov, A. G., Stepanov, A. V., Kliem, B., & Furst, E. 2004, Astron. Lett., 30, 319
Zhang, J., Tian, H., Zarka, P., et al. 2023, ApJ, 953, 65
Zimovets, I. V., McLaughlin, J. A., Srivastava, A. K., et al. 2021, Space Sci. Rev., 217, 66

Appendix A: All flares from the sample

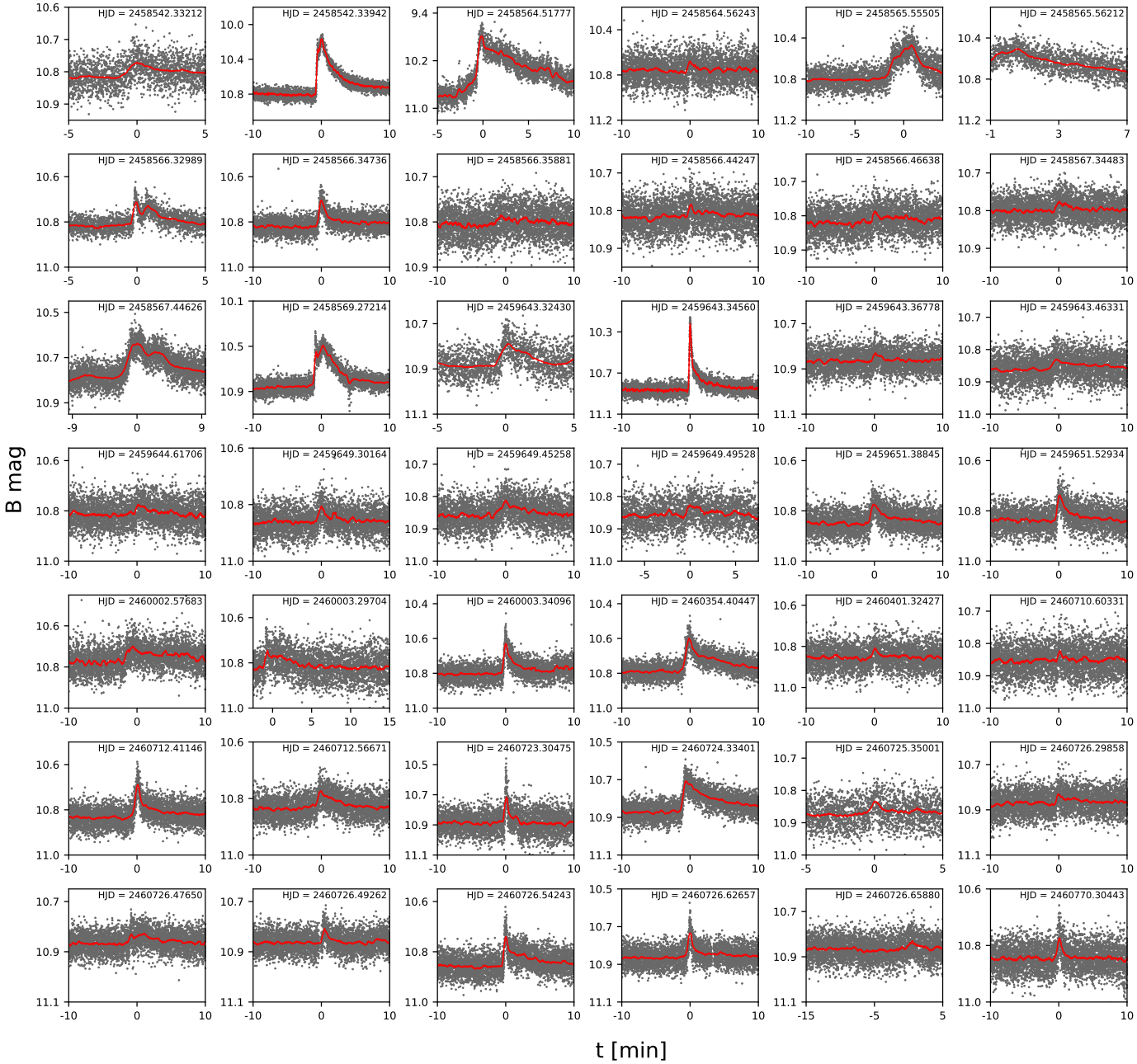

Fig. A.1. Light curves of all detected flares (gray points), smoothed with a Savitzky–Golay filter (red lines). The HJD of each peak is marked in the corresponding panel.

Appendix B: Correlations between the measured flare parameters

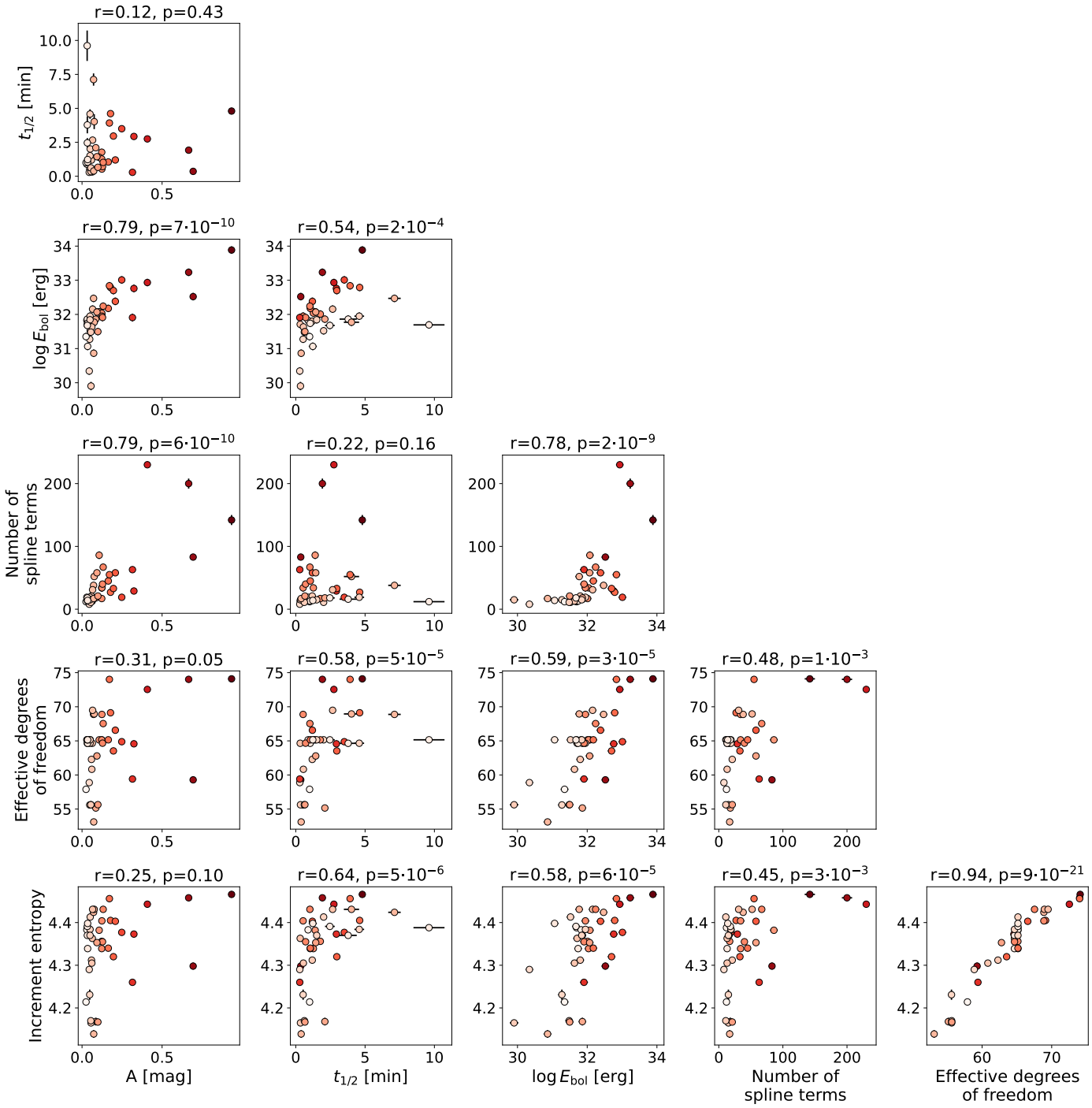

Fig. B.1. Relationships between the measured flare parameters. The color scale indicates the flare amplitude to make the identification easier across different panels. The Spearman rank correlation coefficients and their p-values are shown above each panel.

Appendix C: Observing log

Table C.1. Observing log.

Date	Number of frames	Noise [mag]	Date	Number of frames	Noise [mag]	Date	Number of frames	Noise [mag]
2019-02-23	61000	0.04	2022-03-11	99652	0.04	2024-04-06	1931	0.08
2019-02-26	102000	0.05	2022-03-12	88282	0.04	2024-04-07	30000	0.04
2019-02-27	101000	0.04	2022-03-13	108216	0.08	2024-04-09	22000	0.06
2019-03-21	78027	0.11	2022-03-14	19994	0.07	2024-04-11	23600	0.06
2019-03-22	56000	0.06	2023-01-12	20555	0.06	2024-04-12	25000	0.05
2019-03-23	80000	0.03	2023-01-28	4779	0.05	2024-04-13	26500	0.08
2019-03-24	62000	0.03	2023-01-29	51376	0.05	2024-04-14	28000	0.08
2019-03-26	52899	0.05	2023-02-24	5889	0.06	2025-02-03	91334	0.04
2019-03-27	50000	0.04	2023-02-26	20108	0.05	2025-02-04	22684	0.05
2019-05-18	27653	0.06	2023-02-27	50711	0.05	2025-02-05	100000	0.04
2019-05-20	12149	0.31	2023-03-01	109735	0.05	2025-02-16	83170	0.05
2022-03-04	53672	0.04	2024-02-13	100000	0.04	2025-02-17	87366	0.05
2022-03-05	32431	0.05	2024-02-14	11657	0.08	2025-02-18	110000	0.05
2022-03-06	59619	0.05	2024-03-30	34000	0.06	2025-02-19	120000	0.05
2022-03-07	17887	0.05	2024-03-31	32619	0.06	2025-04-04	10000	0.05
2022-03-08	6104	0.04	2024-04-01	28709	0.08			
2022-03-10	93136	0.04	2024-04-02	33936	0.06			

Appendix D: Flare parameters

Table D.1. Properties of the detected flares.

Peak time [HJD]	Amplitude [mag]	$t_{1/2}$ [min]	E_B [10^{32} erg]	$E_{\rm bol}$ [10^{32} erg]	Number of spline terms	Effective degrees of freedom	Increment entropy
2458542.33212	0.051 ± 0.003	2.01 ± 0.19	0.043 ± 0.001	0.332 ± 0.077	11 ± 2	65.154 ± 0.003	4.413 ± 0.002
2458542.33942	0.666 ± 0.003	1.92 ± 0.02	2.225 ± 0.008	17.113 ± 3.949	200 ± 8	74.018 ± 0.001	4.458 ± 0.001
2458564.51777	0.934 ± 0.005	4.80 ± 0.06	9.974 ± 0.017	76.727 ± 17.706	142 ± 8	74.093 ± 0.109	4.466 ± 0.001
2458564.56243	0.123 ± 0.009	1.77 ± 0.25	0.133 ± 0.006	1.023 ± 0.236	17 ± 3	65.146 ± 0.002	4.356 ± 0.002
2458565.55505	0.324 ± 0.004	2.93 ± 0.07	0.748 ± 0.005	5.757 ± 1.328	29 ± 3	64.571 ± 0.270	4.373 ± 0.004
2458565.56212	0.248 ± 0.005	3.50 ± 0.15	1.332 ± 0.027	10.245 ± 2.364	19 ± 1	64.879 ± 0.150	4.377 ± 0.003
2458566.32989	0.107 ± 0.003	1.40 ± 0.06	0.155 ± 0.003	1.193 ± 0.275	86 ± 6	65.148 ± 0.002	4.382 ± 0.001
2458566.34736	0.123 ± 0.003	1.27 ± 0.05	0.142 ± 0.002	1.094 ± 0.252	34 ± 3	65.150 ± 0.002	4.339 ± 0.001
2458566.35881	0.032 ± 0.001	9.61 ± 1.12	0.064 ± 0.001	0.494 ± 0.114	12 ± 2	65.154 ± 0.002	4.388 ± 0.002
2458566.44247	0.048 ± 0.005	0.53 ± 0.08	0.024 ± 0.001	0.188 ± 0.043	15 ± 1	55.605 ± 0.009	4.231 ± 0.012
2458566.46638	0.030 ± 0.004	0.89 ± 0.17	0.087 ± 0.001	0.670 ± 0.155	19 ± 2	65.149 ± 0.002	4.383 ± 0.005
2458567.34483	0.025 ± 0.003	1.00 ± 0.21	0.029 ± 0.002	0.224 ± 0.052	12 ± 1	57.896 ± 0.005	4.214 ± 0.004
2458567.44626	0.178 ± 0.002	4.61 ± 0.10	0.799 ± 0.009	6.150 ± 1.419	27 ± 2	69.121 ± 0.001	4.405 ± 0.003
2458569.27214	0.408 ± 0.003	2.75 ± 0.04	1.116 ± 0.004	8.586 ± 1.981	230 ± 4	72.540 ± 0.001	4.443 ± 0.001
2459643.32430	0.124 ± 0.007	0.53 ± 0.05	0.115 ± 0.001	0.888 ± 0.205	34 ± 6	68.877 ± 0.128	4.404 ± 0.003
2459643.34560	0.694 ± 0.005	0.36 ± 0.01	0.432 ± 0.008	3.319 ± 0.766	83 ± 3	59.285 ± 0.004	4.298 ± 0.008
2459643.36778	0.064 ± 0.009	0.32 ± 0.07	0.067 ± 0.001	0.513 ± 0.118	13 ± 2	64.649 ± 0.002	4.363 ± 0.003
2459643.46331	0.033 ± 0.003	3.78 ± 0.62	0.095 ± 0.003	0.729 ± 0.168	16 ± 2	64.640 ± 0.003	4.370 ± 0.006
2459644.61706	0.045 ± 0.015	0.29 ± 0.15	0.003 ± 0.003	0.022 ± 0.005	8 ± 3	58.880 ± 0.006	4.290 ± 0.003
2459649.30164	0.059 ± 0.004	1.19 ± 0.14	0.082 ± 0.002	0.631 ± 0.146	21 ± 2	62.282 ± 0.004	4.312 ± 0.002
2459649.45258	0.050 ± 0.002	4.58 ± 0.35	0.116 ± 0.003	0.889 ± 0.205	19 ± 2	64.654 ± 0.001	4.384 ± 0.006
2459649.49528	0.035 ± 0.005	1.04 ± 0.22	0.071 ± 0.003	0.548 ± 0.126	13 ± 2	64.645 ± 0.001	4.339 ± 0.002
2459651.38845	0.086 ± 0.003	2.10 ± 0.13	0.095 ± 0.004	0.727 ± 0.168	18 ± 2	55.157 ± 0.007	4.168 ± 0.009
2459651.52933	0.128 ± 0.005	0.71 ± 0.05	0.106 ± 0.001	0.813 ± 0.188	40 ± 1	64.661 ± 0.001	4.355 ± 0.001
2460002.57683	0.072 ± 0.003	7.12 ± 0.45	0.384 ± 0.006	2.951 ± 0.681	38 ± 3	68.880 ± 0.008	4.424 ± 0.002
2460003.29704	0.076 ± 0.006	4.02 ± 0.55	0.077 ± 0.001	0.590 ± 0.136	52 ± 2	68.948 ± 0.003	4.431 ± 0.002
2460003.34095	0.208 ± 0.008	1.20 ± 0.08	0.314 ± 0.005	2.412 ± 0.557	58 ± 2	66.562 ± 0.002	4.403 ± 0.003
2460354.40447	0.196 ± 0.003	2.96 ± 0.07	0.649 ± 0.001	4.994 ± 1.152	33 ± 3	63.526 ± 0.004	4.320 ± 0.002
2460401.32427	0.061 ± 0.008	0.55 ± 0.11	0.056 ± 0.001	0.431 ± 0.099	13 ± 1	60.832 ± 0.004	4.305 ± 0.002
2460710.60331	0.056 ± 0.008	0.34 ± 0.08	0.001 ± 0.001	0.008 ± 0.002	15 ± 3	55.632 ± 0.006	4.165 ± 0.004
2460712.41146	0.164 ± 0.004	1.05 ± 0.04	0.195 ± 0.003	1.499 ± 0.346	45 ± 2	65.154 ± 0.002	4.340 ± 0.005
2460712.56671	0.066 ± 0.003	2.66 ± 0.18	0.186 ± 0.003	1.429 ± 0.330	31 ± 3	69.482 ± 0.002	4.431 ± 0.002
2460723.30475	0.315 ± 0.011	0.29 ± 0.02	0.105 ± 0.002	0.809 ± 0.187	63 ± 2	59.406 ± 0.003	4.260 ± 0.003
2460724.33401	0.171 ± 0.002	3.92 ± 0.09	0.897 ± 0.005	6.897 ± 1.592	55 ± 3	74.012 ± 0.001	4.456 ± 0.001
2460725.35001	0.055 ± 0.006	0.62 ± 0.18	0.040 ± 0.002	0.304 ± 0.070	11 ± 1	55.632 ± 0.004	4.170 ± 0.006
2460726.29858	0.050 ± 0.005	1.51 ± 0.22	0.091 ± 0.004	0.697 ± 0.161	15 ± 3	65.154 ± 0.002	4.370 ± 0.001
2460726.47650	0.033 ± 0.003	2.46 ± 0.35	0.062 ± 0.001	0.476 ± 0.110	18 ± 2	65.149 ± 0.009	4.391 ± 0.002
2460726.49285	0.073 ± 0.007	0.39 ± 0.05	0.009 ± 0.001	0.073 ± 0.017	17 ± 1	53.114 ± 0.002	4.139 ± 0.009
2460726.54243	0.132 ± 0.004	1.02 ± 0.05	0.227 ± 0.004	1.743 ± 0.402	67 ± 3	67.534 ± 0.003	4.431 ± 0.002
2460726.62657	0.093 ± 0.005	1.44 ± 0.12	0.153 ± 0.003	1.174 ± 0.271	58 ± 1	62.788 ± 0.001	4.353 ± 0.003
2460726.65880	0.035 ± 0.003	1.23 ± 0.29	0.015 ± 0.001	0.116 ± 0.027	14 ± 3	65.154 ± 0.006	4.398 ± 0.001
2460770.30443	0.099 ± 0.006	0.66 ± 0.06	0.041 ± 0.001	0.314 ± 0.072	21 ± 1	55.645 ± 0.004	4.167 ± 0.004

Notes. The E_B errors only include the uncertainty of ED, while the $E_{\rm bol}$ errors also include the uncertainty of the conversion from Eq. 2.